THE ASTROPHYSICAL JOURNAL, 445:666–679, 1995 June 1

ROSAT OBSERVATIONS OF NGC 2146: EVIDENCE FOR A STARBURST-DRIVEN SUPERWIND

L. ARMUS,[1,2] T. M. HECKMAN,[3] K. A. WEAVER,[4] AND M. D. LEHNERT[2,5]

Received 1994 July 26; accepted 1994 December 9

ABSTRACT

We have imaged the edge-on starburst galaxy NGC 2146 with the Position Sensitive Proportional Counter (PSPC) and the High Resolution Imager (HRI) on board *ROSAT* and have compared these data to optical images and long-slit spectra. NGC 2146 possesses a very large X-ray nebula with a half-light radius of 1′ (4 kpc) and a maximum diameter of ∼4′, or 17 kpc. The X-ray emission is resolved by the PSPC and preferentially oriented along the minor axis, with a total flux of 1.1×10^{-12} ergs cm^{-2} s^{-1} over 0.2–2.4 keV and a luminosity of $\sim 3 \times 10^{40}$ ergs s^{-1}. The inner X-ray nebula is resolved by the HRI into at least four bright knots together with strong diffuse emission responsible for at least 50% of the flux within a radius of 0.5 (∼2 kpc). The brightest knot has a luminosity of (2–3) $\times 10^{39}$ ergs s^{-1}. The X-ray nebula has a spatial extent much larger than the starburst ridge seen at centimeter wavelengths by Kronberg & Biermann (1981) and is oriented in a "X-like" pattern along the galaxy minor axis at a position angle of ∼30°. This minor-axis X-ray emission is associated with a region of Hα and dust filaments seen in optical images. Optical spectra show that the emission-line gas along the minor axis is characterized by relatively broad lines (∼250 km s^{-1} FWHM) and by "shocklike" emission-line flux ratios. Together with the blue-asymmetric nuclear emission-line and NaD interstellar absorption-line profiles, these optical data strongly suggest the presence of a starburst-driven superwind. The X-ray spectrum extracted from the central 5′ contains a strong Fe L emission-line complex at 0.6–1.0 keV and a hard excess above 1.0 keV. The spectrum is best described with a two-component model, containing a soft ($kT \sim$ 400–500 eV) Raymond-Smith thermal plasma together with either a $\Gamma = 1.7$ power-law or a $kT > 2.2$ keV bremsstrahlung component. The soft thermal component provides ∼30% of the total luminosity over 0.2–2.4 keV, or $\sim 10^{40}$ ergs s^{-1}. The pressure derived from the soft component of the X-ray spectrum is consistent with that predicted from a starburst-driven superwind if the filling factor of the warm gas is ∼1%–10%. If the hard X-ray component is thermal gas associated with the galactic outflow, the filling factor must be close to unity. Predictions of the luminosity, temperature, and size of an adiabatic starburst-generated windblown bubble are consistent with those measured for the soft thermal X-ray emission in NGC 2146. The hard X-ray component, however, has a luminosity much larger than predicted by the superwind model if this component is thermal emission from gas heated by an internal shock in the expanding bubble. We briefly review various possibilities as to the nature of the hard X-ray component in NGC 2146.

Subject headings: galaxies: individual (NGC 2146) — galaxies: starburst — X-rays: galaxies

1. INTRODUCTION

The nearby ($D = 14.7$ Mpc), edge-on ($i \sim 25°$) spiral galaxy NGC 2146 exhibits ample evidence at optical, infrared, and radio wavelengths for a nuclear starburst. A luminous, $L_{FIR} = 6.3 \times 10^{10}\ L_\odot$, warm $S_{60}/S_{100} = 0.8$ *IRAS* source, NGC 2146, also contains a large reservoir of molecular gas, with $\sim 6 \times 10^9$ $M_\odot$ of H_2 within the central kiloparsec (Young et al. 1988). Nuclear optical-line ratios similar to those found for galactic H II regions and a strong, narrow, nuclear Bγ line (4×10^{-13} ergs s^{-1}) indicate a large population of hot young stars. Near-infrared $J-H$ and $H-K$ colors suggest that hot ($T \geq 600$ K) dust contributes at least 30%–40% of the light in the K bandpass (Hutchings et al. 1990). At 6 cm, Kronberg & Bierman (1981) find an extended ridge of nonthermal emission over a 6″ × 40″ (0.4 × 2.9 kpc) region and a nuclear "triple" source in the central 5″ (∼350 pc), both of which roughly align with the galaxy major axis.

In addition to the central starburst, a galactic outflow may be present in NGC 2146. Such an outflow occurs when the hot gas bubble produced by a large number of supernova remnants expands outward along the largest pressure gradient—generally the minor axis. Long-slit optical spectra (Armus, Heckman, & Miley 1989, hereafter AHM89; Hutchings et al. 1990) show that, although the nuclear emission lines are indicative of ionization by hot stars, those up to 15″ east of the nucleus resemble lines produced in objects which are shock-heated, i.e., very strong [O I], [N II], and [S II] lines relative to Hα. In addition, a $B-R$ color map (Hutchings et al.) shows several dust filaments emerging from the nucleus along the minor axis. These dust filaments extend along the minor axis out to a radius of ∼2 kpc and resemble the spectacular dust plumes seen in the region of outflow in the starburst galaxy NGC 1808 (Phillips 1993). Recent low-resolution VLA observations of NGC 2146 show a diffuse radio synchrotron halo surrounding the central starburst (Lehnert et al. 1995). Similar radio halos are present in the prototype starburst/superwind

[1] Palomar Observatory, California Institute of Technology, 320-47, Pasadena, CA 91125.

[2] Visiting Astronomer, Kitt Peak National Observatory, operated by the Association of Universities for Research in Astronomy, Inc., under contract with the National Science Foundation.

[3] Department of Physics, Johns Hopkins University, Homewood Campus, Baltimore, MD 21218; and Adjunct Astronomer, Space Telescope Science Institute.

[4] Department of Astronomy and Astrophysics, 525 Davey Lab, Pennsylvania State University, University Park, PA 16802.

[5] Institute of Geophysics and Planetary Physics, Lawrence Livermore National Laboratory, P.O. Box 808, L-413, Livermore, CA 94551.

systems M82 and NGC 253 and are thought to be produced by relativistic plasma created by supernovae in the starburst and then convected out into the halo by the galactic wind (cf. Seaquist & Odegard 1991).

In a starburst nucleus with an outflowing wind, X-rays can be expected primarily from high-mass binaries, from supernova remnants, and from extended, hot ($T \sim 10^7$ K), shock-heated ambient gas (see Heckman, Lehnert, & Armus 1993, hereafter HLA93, for a review of the latter process). The nearby, well-studied starburst galaxies M82, NGC 253, and NGC 3628 have large, asymmetric X-ray halos which have been attributed to nuclear winds escaping along their minor axes (Fabbiano 1988; Fabbiano, Heckman, & Keel 1990). Given the evidence for both a nuclear starburst and an expanding wind in NGC 2146, we have used the *ROSAT* High Resolution Imager (HRI) and Position Sensitive Proportional Counter (PSPC) to search for the X-ray emission expected from such a system and to place contraints on its morphology and spectral characteristics. In addition, we have obtained new optical long-slit spectra along the major and minor axes of NGC 2146 to provide a complimentary probe of the physical and dynamical state of the interstellar gas in the regions where the X-rays are emitted.

2. OBSERVATIONS AND DATA REDUCTION

2.1. *X-Ray*

NGC 2146 was observed on 1992 February 25 with the PSPC experiment on board *ROSAT*. The total, vignetting-corrected effective on-source exposure time was 5954 s. The galaxy was well positioned at the center of the field of view of the instrument, with essentially all its X-ray flux contained within the central 4′.0 (see below).

ROSAT HRI observations of NGC 2146 were carried out over 1992 March 13–14 for a total live-time integration of 5393 s. As with the PSPC observation, NGC 2146 was, to within the pointing accuracy, centered in the HRI field of view. The complex morphology of NGC 2146 is resolved with the HRI, with a total extent of ~1′.0.

2.2. *Optical*

Long-slit optical spectra were taken on the night of 1994 January 12, using the KPNO 4 m in combination with the Ritchey-Chrétien (RC) spectrograph. The RC spectrograph was equipped with a Tektronics CCD and the KPC-24 860 line mm^{-1} grating. The resolution was 1.3 Å and the usable slit length was greater than 5′ at a spatial resolution of ~0″.69 $pixel^{-1}$. The slit width of 2″.0 was well matched to the seeing at the time of the observations (~1″.9 FWHM). Four exposures were taken, two along the NGC 2146 minor axis (P.A. ~ 55°) and two along the major axis (P.A. ~ 145°). Each was 1800 s and centered on the brightest portion of the bulge of the galaxy as seen through the slit-viewing camera. The spectra discussed in this paper are an average of each pair. The data were flat-fielded using dome flat-field exposures and bias-subtracted using an average of 15 bias frames and scaled using the CCD overscan region. The data were flux-calibrated using spectra of Hiltner 102 taken using a 10″-wide slit. The line fluxes, line widths, and redshifts of the emission lines were measured using the task SPLOT of the NOAO's IRAF package. Spectra were extracted in bins of 2″.1 along the slit.

Lower resolution (~13 Å) long-slit spectra obtained on the night of 1988 January 14 with the RC spectrograph coupled with a TI CCD on the KPNO 4 m telescope are also presented here. A 2″.0-wide slit oriented at P.A. ~ 40° and P.A. ~ 133° were used, lying approximately along the minor and major axes, respectively. The nuclear spectrum has been discussed in AHM89 along with a full description of the data reduction process.

Optical broadband *R* and narrowband Hα + [N II] images, taken from Armus, Heckman, & Miley (1990) are also presented here for comparison to the *ROSAT* HRI data. These optical data were obtained at the Cassegrain focus (f/7.5) of the KPNO 2.1 m telescope. The scale for these images is 0″.38 $pixel^{-1}$. A full description of the data reduction procedure is given in Armus et al. (1990).

3. RESULTS

3.1. *X-Ray Morphology*

3.1.1. *PSPC*

The central 12′ of the full-channel *ROSAT* PSPC image of NGC 2146 is displayed in Figure 1. For this image we have blocked the original data into 3″.0 pixels then smoothed the resulting image by a $\sigma = 5$ pixel Gaussian for a final effective resolution of ~45″ FWHM. The PSPC contours are overlayed on a gray-scale representation of the Palomar Observatory Sky Survey (POSS) *J* plate extracted from the digitized version available at the Space Telescope Science Institute. Within the pointing accuracy of the X-ray telescope (~5″), the centroid of the X-ray emission is well aligned with the optical/infrared nucleus (Benvenuti, Capaccioli, & D'Odorico 1975). The X-ray

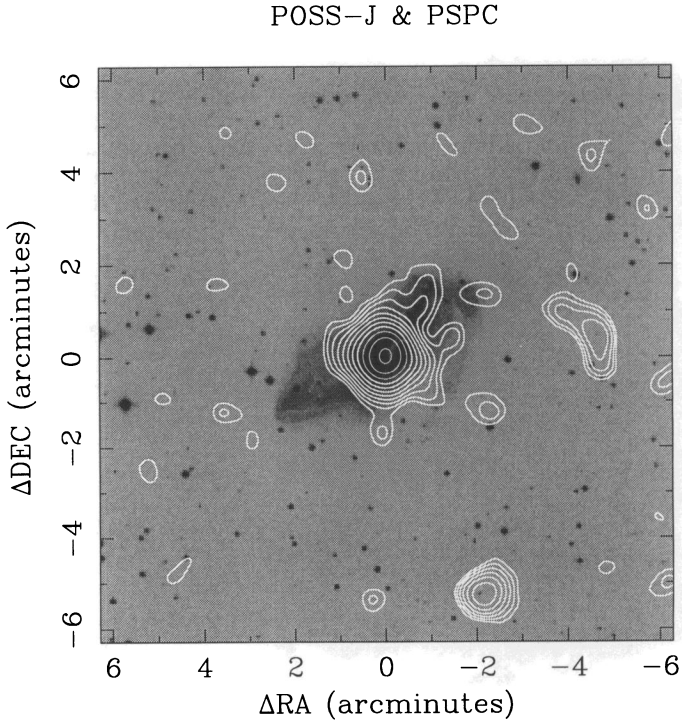

FIG. 1.—Gray-scale POSS *J* plate image generated from the STScI digital sky survey with overlayed contours of the *ROSAT* PSPC image of NGC 2146 in white. The PSPC image has been generated from the raw PSPC data first by blocking into 3″.0 pixels than by smoothing with a Gaussian with $\sigma = 5$ pixels. Contours are logarithmic, progressing from 9 counts $arcmin^{-2}$ (~2.5 σ) to 310 counts $arcmin^{-2}$ (maximum), each level being a factor of 1.4 greater than the previous level. As in all the following figures, north is up and east is to the left.

nebula in NGC 2146 is very large, with a half-light diameter of ~ 1 and a maximum size of 4′. At the distance of NGC 2146, these correspond to 4.3 and 17.3 kpc, respectively, for $H_0 = 75$ km s^{-1} Mpc^{-1}. Although the bright starburst nucleus is unresolved by the PSPC, the X-ray emission as a whole is clearly resolved (see Fig. 2). Two-component thermal plasma fits to the extracted PSPC spectrum (see below) deliver a total flux of $\sim 1.1 \times 10^{-12}$ ergs cm^{-2} s^{-1} over the 0.2–2.4 keV range, after correcting for an absorbing neutral hydrogen column density of 7.3×10^{20} cm^{-2}.

Along with the primary galactic component there are two other features within the central 12′ field. Approximately 4′–5′ to the west of the nucleus there is a faint, resolved "tail" of X-ray emission that is apparently connected to NGC 2146 at the lowest flux levels. There is no stellar emission at this location in the POSS, and determination of the true nature of this X-ray feature will have to await a much deeper image of the NGC 2146 system. As well as this faint, curving tail there is a relatively strong unresolved source of X-rays $\sim 5'$–$6'$ to the south of NGC 2146. This feature has no obvious, bright optical counterpart on the POSS and may possibly be associated with a faint, background galaxy cluster or QSO.

In Figure 2 we compare the azimuthally averaged surface brightness profile of NGC 2146 to a scaled representation of the on-axis point-spread function (PSF) of the PSPC. For the PSF we have used the high signal-to-noise ratio (1.8 ks) AO1 observation of Mrk 509, an unresolved Seyfert type 1 galaxy which provides an accurate in-flight measurement of the on-axis PSF at the time of the NGC 2146 observations (Hasinger et al. 1992). Beyond a radius of $\sim 0.'75$–$1.'0$ there is a clear excess of counts in the NGC 2146 data over that expected from a completely unresolved source seen in the PSPC.

3.1.2. *HRI*

In the high-resolution HRI image the inner X-ray nebula in NGC 2146 breaks up into a group of at least four bright knots together with strong diffuse emission over the central 1′–1.′5 (Fig. 3). There is a "tongue" or jet of X-ray emission which extends $\sim 30''$ to the southeast of the strong central source (A in Fig. 3*c*), as well as fainter "fingers" of emission along the southeast and southwest directions, coincident with sources C and D. Overall the nebula has an "X" pattern over the central 1′ region with an orientation roughly perpendicular to the optical major axis. The brightest two sources, labeled A and B in Figure 3*c*, account for $\sim 30\%$ of the total flux in the HRI image, after fitting suitably scaled versions of the on-axis PSF to the data. Although the HRI has essentially no spectral capabilities, the size of the HRI image in Figure 3 corresponds to the half-light diameter of the PSPC data, and we have therefore used the spectrally derived fluxes of the latter to estimate that source A has a 0.2–2.4 keV luminosity of $\sim (2$–$3) \times 10^{39}$ ergs s^{-1}. This is comparable to the most powerful high-mass X-ray binary source known, SMC X-1, and to the most luminous known individual extragalactic supernova remnants (cf. Schlegel 1994, and references therein). However, since the HRI beam covers ~ 300–400 pc at the distance of NGC 2146, source A may be made up of more than a single nuclear X-ray source.

In Figures 3*b* and 3*c* we display the *ROSAT* HRI data overlayed on an Hα + [N II] image from Armus et al. (1990) along with an illustration of the size and position of the nonthermal 6 cm radio ridge mapped by Kronberg & Biermann (1981). This radio emission is drawn as a rectangular region oriented at P.A. $\sim 128°$ in Figure 3*c*. Note that, although there is an ambiguity in the exact alignment between the X-ray and radio emission due to the uncertainty in the absolute astrometry of the *ROSAT* data, we have positioned the HRI and 6 cm maps as in Figure 3*c* because (1) the nominal X-ray centroid is consistent with the radio nucleus to within the pointing uncertainties, (2) the central X-ray source and tongue of emission to the southeast have a position angle and morphology similar to the radio ridge, and (3) we expect a close association between the X-ray and radio emission in the radio ridge which defines the position of the central starburst and marks the location of bright supernovae and supernova remnants. We have aligned the X-ray and radio centroids in Figure 3*c* and used the offset between the radio and optical/infrared nuclei to position the HRI map and the Hα + [N II] map of Figure 3*b*. The most striking feature of Figure 3*c* is that the X-ray emission has a much larger extent than the central starburst ridge, and this extension is primarily along the starburst's (radio ridge's) minor axis. Since the strongest identifiable sources (A–D) account for less than 50% of the X-ray flux, most of this emission is diffuse in nature (implying a large reservoir of warm gas—see below). While we cannot rule out a collection of well-separated ($\Delta R < 4''$–$5''$) evenly spaced point sources masquerading as true diffuse emission, such a possibility seems unlikely.

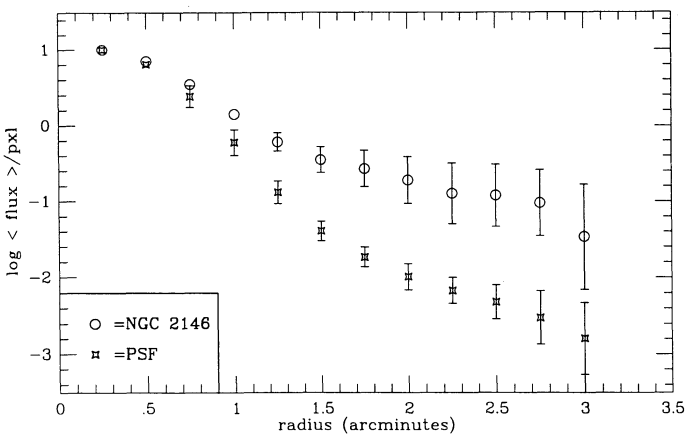

FIG. 2.—Comparison of the azimuthally averaged radial surface brightness profile of NGC 2146 with that of the on-axis PSF of the PSPC at the time of the observations. The latter is represented by the high signal-to-noise ratio observation of the Seyfert 1 galaxy Mrk 509. The vertical axis is in normalized logarithmic flux units. Error bars are given only when the standard deviation in the mean in an individual radial bin is greater than the size of the point used to trace the profiles.

3.2. *X-Ray Spectrum*

From the PSPC data, we have extracted a spectrum of NGC 2146 over the central 5′ using the task QPSPEC in the NOAO's IRAF data reduction package. Although we believe the tail $\sim 4'$ to the west of the NGC 2146 nucleus is associated with the galaxy, we have explicitly excluded it from the extraction to make interpretation of the dominant X-ray nebula less ambiguous. The PSPC background was determined from an annular region of 6′–8′ radius centered on NGC 2146.

The extracted spectrum contains 426 total counts, binned up into 25 PHA channels such that each channel contains at least 10 counts. We have fitted this spectrum with a number of models using the XSPEC reduction package (Shafer, Haberl, & Arnaud 1989). With a reduced χ^2 of 1.5 for 20 degrees of freedom (dof), a single-temperature Raymond-Smith thermal

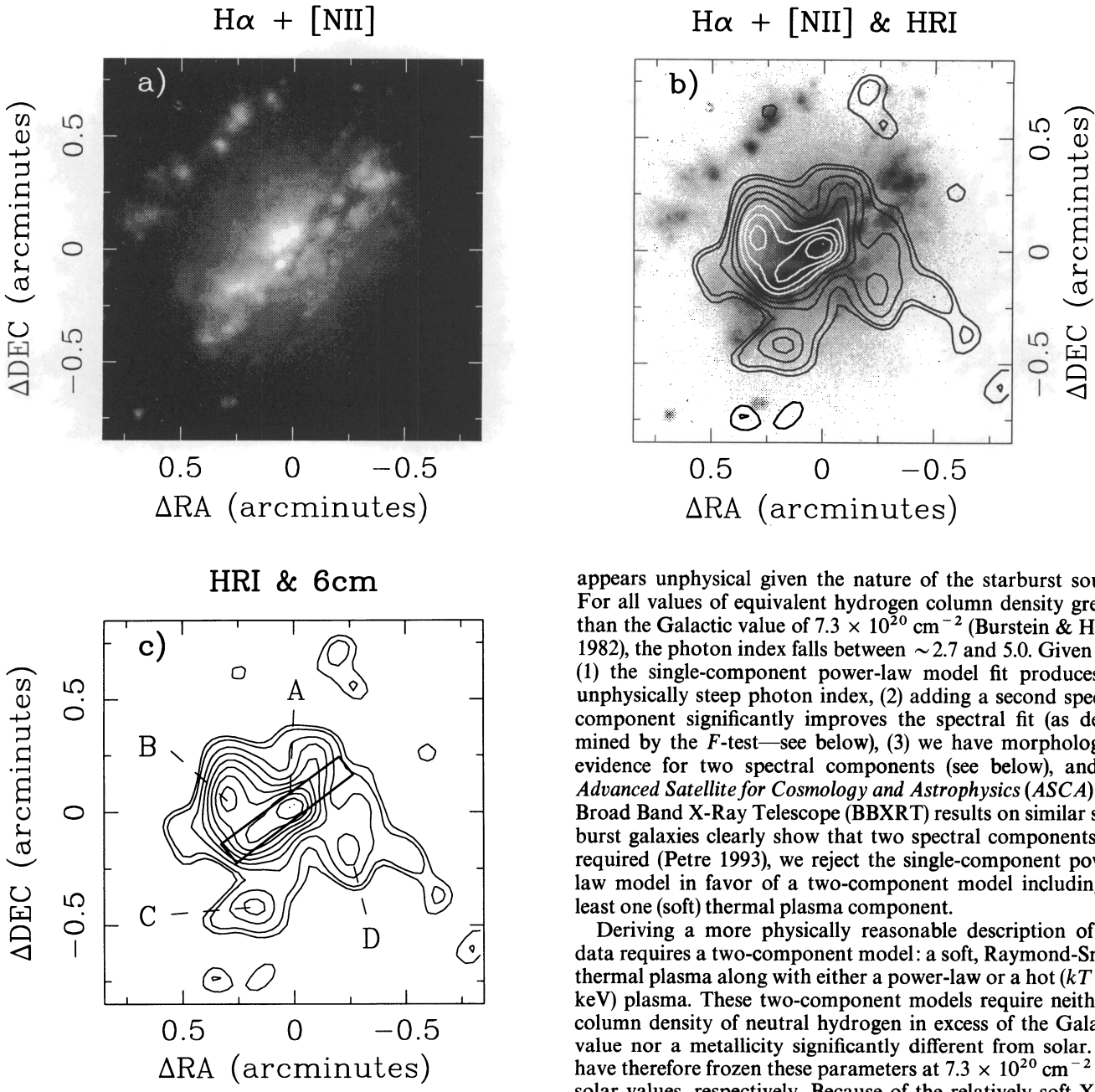

FIG. 3.—Comparison of the *ROSAT* HRI image of NGC 2146 with the Hα + [N II] image from Armus et al. (1990) and the nonthermal radio (starburst) ridge from Kronberg & Biermann (1981). The *ROSAT* HRI data has been blocked into 2.″0 pixels before being smoothed with a $\sigma = 2$ pixel Gaussian. A gray-scale representation of the Hα + [N II] image is shown in (*a*), with the *ROSAT* HRI contours overlayed in (*b*). In (*c*) the brightest four X-ray sources (A–D) are labeled. These sources are discussed in the text. The 6 cm radio ridge is sketched as a 6″ × 40″ rectangle at a P.A. ~ 128° in (*c*) to illustrate the size and orientation of the starburst region. In (*b*) and (*c*) the contours are linear, progressing from 62 counts arcmin^{-2} (~3 σ) to 407 counts arcmin^{-2} (maximum) in steps of 2 σ.

plasma (Raymond & Smith 1977) does not provide an acceptable fit to the data. A single-component power-law model cannot be ruled out (reduced $\chi^2 = 1.1$ for 20 dof), but it requires an unusually steep photon index of $\Gamma \sim 3.4$. This is much larger than expected from an inverse Compton scattering model (see below), where Γ should be equal to 1.7, and appears unphysical given the nature of the starburst source. For all values of equivalent hydrogen column density greater than the Galactic value of 7.3×10^{20} cm^{-2} (Burstein & Heiles 1982), the photon index falls between ~2.7 and 5.0. Given that (1) the single-component power-law model fit produces an unphysically steep photon index, (2) adding a second spectral component significantly improves the spectral fit (as determined by the *F*-test—see below), (3) we have morphological evidence for two spectral components (see below), and (4) *Advanced Satellite for Cosmology and Astrophysics* (*ASCA*) and Broad Band X-Ray Telescope (BBXRT) results on similar starburst galaxies clearly show that two spectral components are required (Petre 1993), we reject the single-component power-law model in favor of a two-component model including at least one (soft) thermal plasma component.

Deriving a more physically reasonable description of the data requires a two-component model: a soft, Raymond-Smith thermal plasma along with either a power-law or a hot ($kT > 2$ keV) plasma. These two-component models require neither a column density of neutral hydrogen in excess of the Galactic value nor a metallicity significantly different from solar. We have therefore frozen these parameters at 7.3×10^{20} cm^{-2} and solar values, respectively. Because of the relatively soft X-ray response of *ROSAT*, there is little leverage on the shape of the hard component which we find necessary to fit the NGC 2146 spectrum above ~1.2 keV. However, recent BBXRT results (Petre 1993) suggest that in the starburst galaxies M82 and NGC 253, there is a very strong hot ($kT \sim 10$ keV) thermal component which dominates the spectra in the hard energy channels. Furthermore, in dusty, infrared-luminous galaxies, such as NGC 2146, we may expect a contribution to the X-ray spectrum from infrared photons Compton-scattered off relativistic electrons in a radio "halo" convected out by the expanding wind (Schaaf et al. 1989). Indeed, low-resolution VLA observations (Lehnert et al. 1995) show a diffuse radio synchrotron halo surrounding the central starburst in NGC 2146. The X-ray spectral signature of the Compton-scattered infrared photons should have a power-law shape with a photon index of $\Gamma = 1.7$. We have therefore fitted the NGC

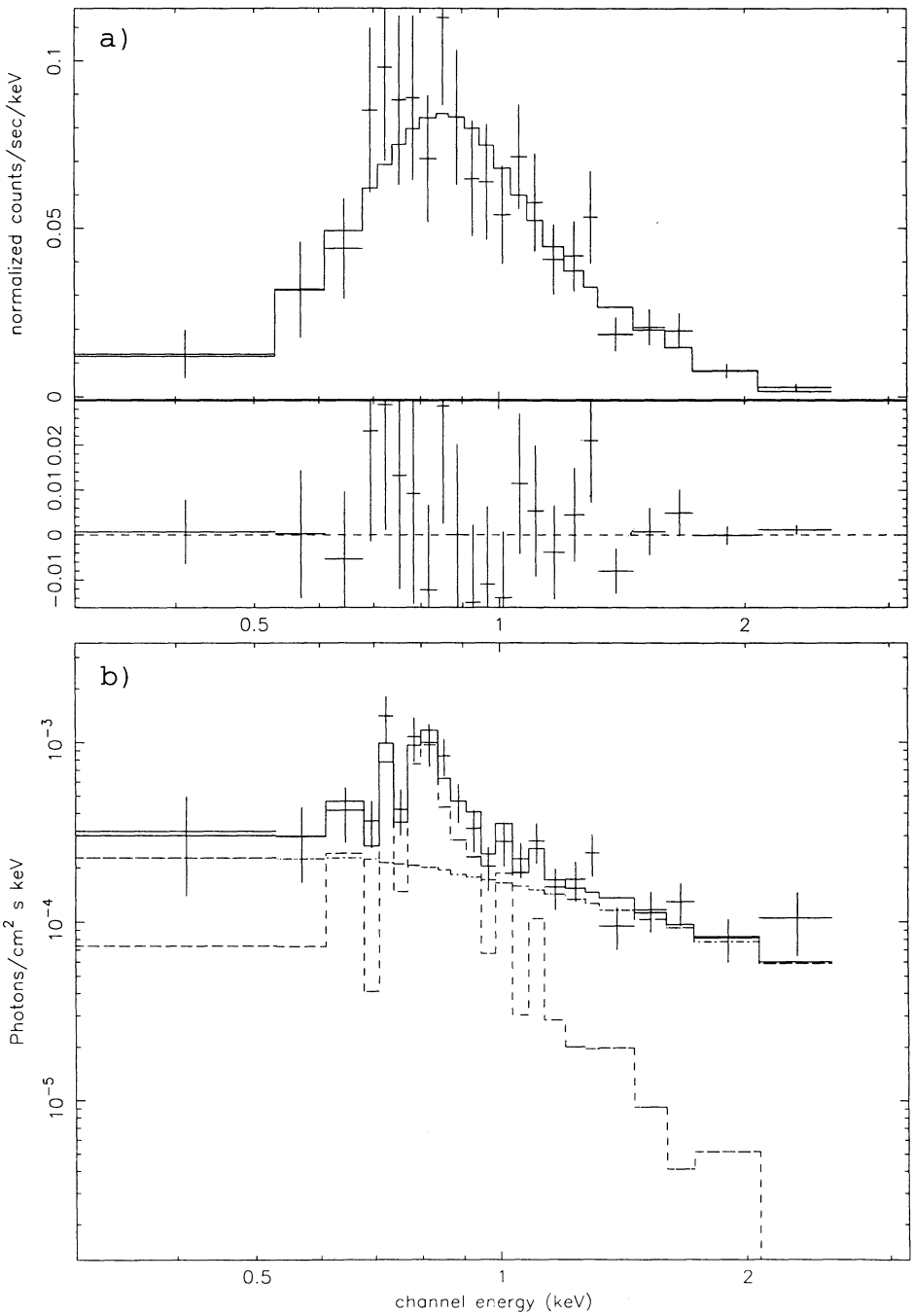

FIG. 4.—Best-fit composite (soft plus hard) thermal plasma fit to the PSPC spectrum extracted from the central ~5′ region around NGC 2146. (*a*) Composite fit along with the residuals; (*b*) unfolded spectrum with the dashed line representing the soft (kT = 400–500 eV) thermal Fe L line emitting plasma and the dash-dotted line representing the hot (kT = 10 keV) bremsstrahlung component used to fit the hard X-ray excess. See text for a complete description of the fitting procedure. (*c*) Single-component power-law fit to the soft (0.1–0.6 keV) and hard (1.0–2.4 keV) PSPC spectrum to highlight the strong excess between 0.6 and 1.0 keV identified with the Fe L line complex.

2146 spectrum with a soft thermal, Raymond-Smith plasma coupled with either a hot (kT = 10 keV) bremsstrahlung or a Compton-scattered (Γ = 1.7) power law. In both cases the normalization of the hard component was left variable but either the temperature of the plasma (in the hot bremsstrahlung model) or the photon index of the power law was fixed during the spectral-fitting procedure. For both of these two-component models an *F*-test (Bevington 1969) shows that the fit to the data has been improved at better than the 99.9% confidence level compared to the single-temperature Raymond-Smith model and at the 99.6% confidence level compared to the pure power-law model. In the two-component models, the soft Raymond-Smith plasma has $kT \sim$ 400–500 eV and carries ~30%–40% of the total X-ray flux seen by *ROSAT*.

In Figures 4*a* and 4*b*, we display our best-fit two-component thermal plasma model. Here, the temperature of the soft Raymond-Smith component is 0.4 ± 0.1 keV, and the reduced χ^2 = 0.7 for 20 dof. In this model the unabsorbed fluxes (the

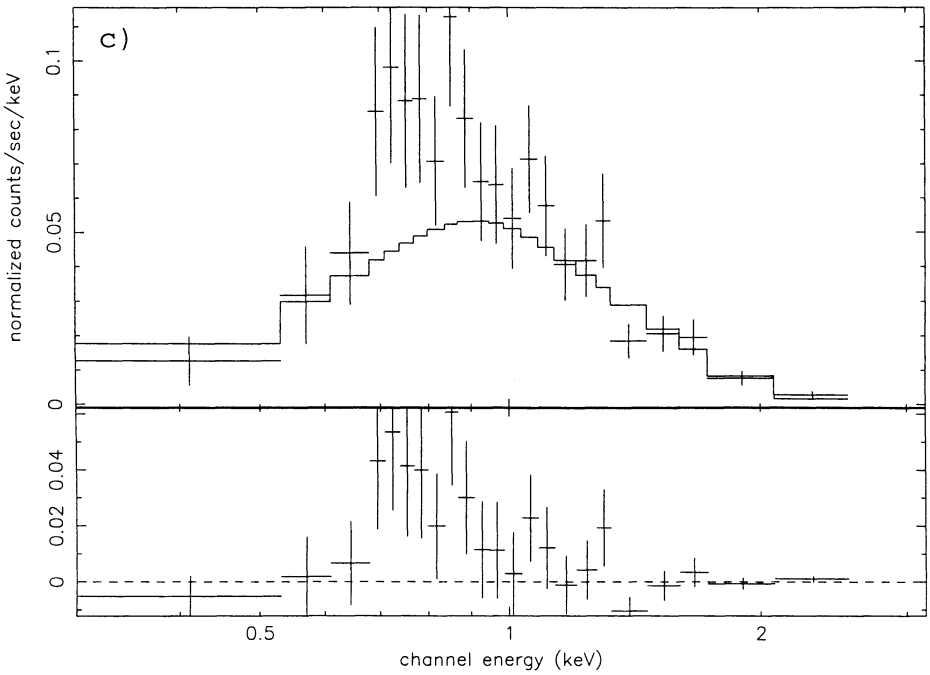

FIG. 4—*Continued*

fluxes after correcting for the Galactic neutral hydrogen column of 7.3×10^{20} cm^{-2}—hereafter the $N_H = 0$ fluxes) in the soft and hard plasmas over 0.2–2.4 keV are 3.9×10^{-13} ergs cm^{-2} s^{-1} and 7.0×10^{-13} ergs cm^{-2} s^{-1}, respectively, corresponding to luminosities of $\sim 10^{40}$ ergs s^{-1} and $\sim 2 \times 10^{40}$ ergs s^{-1}. The composite spectral fit is shown in Figure 4*a*, while the unfolded spectrum, highlighting the contributions of the separate components, is shown in Figure 4*b*. The hot thermal component actually dominates the spectrum both above ~1 keV and also below ~0.5 keV. The soft thermal component is important over ~0.6–1.0 keV where the Fe L emission complex is clearly visible. Note that, although we have displayed the twin thermal plasma fit to the data in Figures 4*a* and 4*b*, the soft plasma plus power-law model provides an equally good fit to the spectrum. Since the second spectral component (the hot plasma or the power law) is seen to dominate the PSPC spectrum both in the lowest and the highest energy channels, we show an example of a single power-law fit to the 0.2–0.6 keV and 1.0–2.4 keV energy channels in Figure 4*c*. A clear positive residual in the energy range between ~0.6 and 1 keV can be seen. This excess is easily explained as emission from the Fe L complex.

Since the NGC 2146 X-ray spectrum requires the presence of both a soft and hard component, we have attempted to generate a pair of images from the PSPC data that isolate these two components to search for any morphological differences. From the PSPC data we have created an "Fe L image" isolating the 0.6–1.0 keV spectral range where the plasma emission lines dominate the spectrum. For comparison, we have also created a "hard" component image drawn from the 1.0–2.4 keV spectral data. In Figures 5*a*–5*d* we display these images at two different resolutions. The "Fe L" (Figs. 5*a* and 5*c*) and "hard" (Figs. 5*b* and 5*d*) X-ray images have been blocked into 7.″5 pixels, but the images in Figures 5*a* and 5*b* have been smoothed with a Gaussian function producing a final resolution of ~35″ FWHM, while the images in Figures 5*c* and 5*d* have been similarly smoothed to a final resolution of ~45″ FWHM. Although both sets of images have strong nuclear components (note the north-south elongation in Figs. 5*a* and 5*b*), the Fe L emission-line images show faint, diffuse emission to the northeast and southwest of the nucleus at the lowest contour levels which are not apparent in the "hard" images. The Fe L PSPC images are reminiscent of the HRI images of Figure 3, except the scale here is much larger, extending out to radii of ~2′, or ~9 kpc. Comparing the surface brightness profiles of the "Fe L" and "hard" images in Figures 5*a* and 5*b*, we find that the former is a factor of between 2.5 and 3.5 brighter than the latter (after normalizing to the peak surface brightness in each image) at radii of 0.′5–1.′2 along the minor axis. Along the major axis the two images are comparable. The soft and hard spectral components required to adequately fit the PSPC data actually have a physical basis in NGC 2146, displaying different morphologies on the 2′–3′ scale.

3.3. *Optical Spectra*

We have used both the low-dispersion spectra in AHM89 and the new higher dispersion spectra described in § 2.2 to provide a complementary probe of the physical and dynamical state of the interstellar gas in the region in which the X-rays are emitted in NGC 2146.

From the AHM89 data we have extracted a nuclear spectrum and off-nuclear spectra along the major and minor axes. The minor-axis off-nuclear spectrum is taken from the regions 6″–28″ northeast and 15″–25″ southwest of the nucleus, while the major-axis spectrum is taken from the regions 11″–24″ southeast and 22″–29″ northwest of the nucleus. In Table 1 we present the most important optical diagnostic line ratios for the three regions (nucleus, off-nuclear major, off-nuclear minor). Note that the [O III] λ5007/Hβ and Hα/Hβ line flux ratios are both upper limits due to the significant effect of the underlying stellar absorption feature on the Hβ emission line.

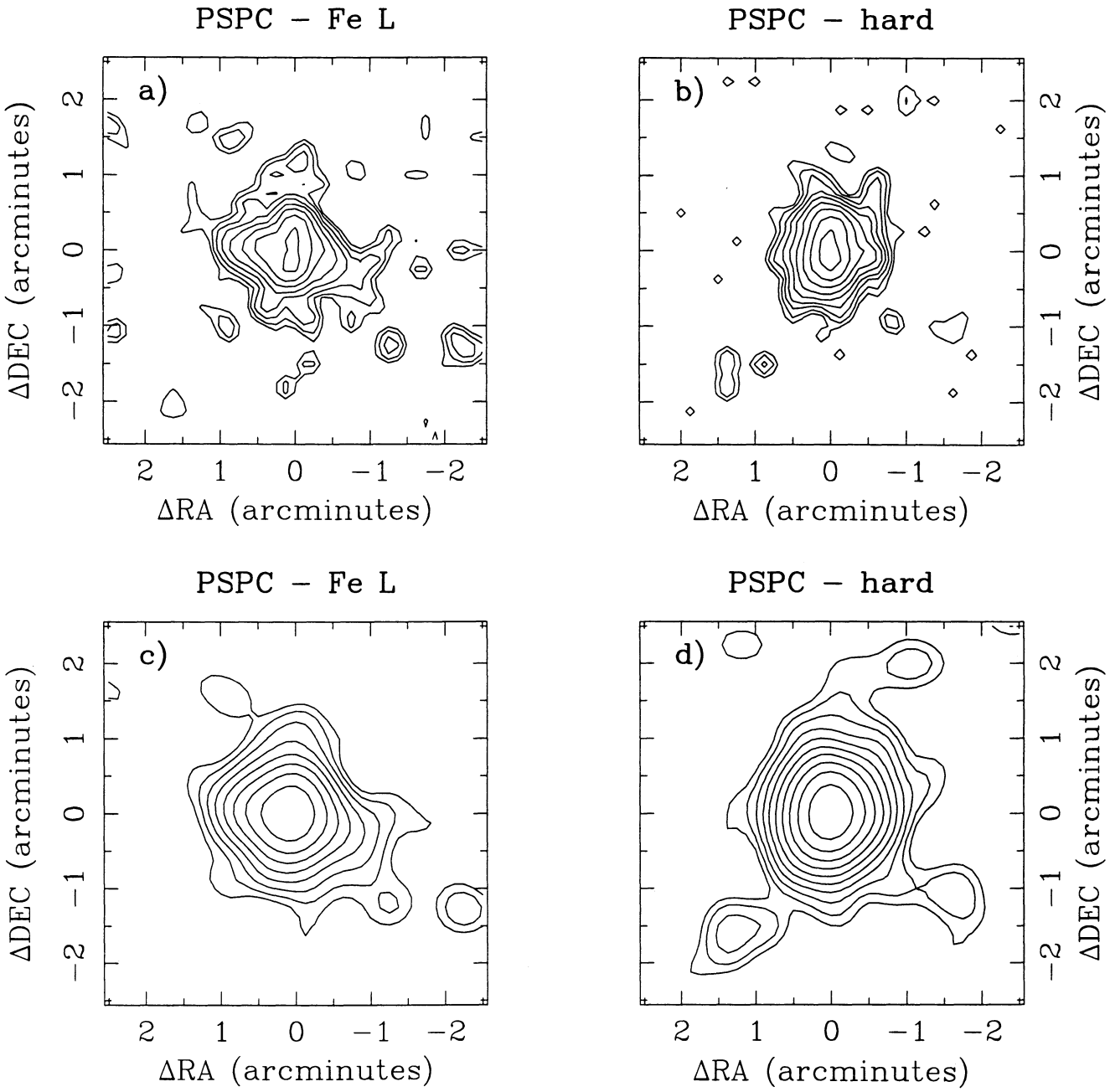

FIG. 5.—Soft (0.6–1.0 keV) and hard (greater than 1.0 keV) images made over appropriate channels of the PSPC data from Fig. 1. The images in (*a*) and (*b*) have been blocked into 7.″5 pixels and then smoothed with a $\sigma = 1$ pixel Gaussian. The images in (*c*) and (*d*) have the same pixel size as the images in (*a*) and (*b*), but have been smoothed with a $\sigma = 2$ pixel Gaussian. In all cases the lowest contour is at the 3 σ level, and contours increase by a factor of 1.5 at each successive level. The lowest levels range over 3–11 counts arcmin^{-2}, and the highest over 111–197 counts arcmin^{-2}.

Such stellar Balmer absorption lines are due to the presence of a significant intermediate-age (10^8–10^9 yr) stellar population. Comparing the [O III] λ5007/Hβ, [O I] λ6300/Hα, [N II] λ6584/Hα, and [S II] $\lambda\lambda$6717+6731/Hα line flux ratios to those empirically classified by Veilleux & Osterbrock (1987), it is clear that while both the nuclear and off-nuclear major-axis spectra have ratios consistent with photoionization by hot stars, the off-nuclear minor-axis spectrum possesses emission-line flux ratios strongly resembling those seen in objects that are shock-heated (e.g., supernova remnants, Herbig-Haro objects, and possibly LINERs—see AHM89 for details).

To examine this in greater detail, we have used our new higher resolution spectra to measure the spatial variation of the [O I]/Hα, [N II]/Hα, and [S II]/Hα emission-line flux ratios along the major and minor axes. The results are shown graphically in Figure 6. The abrupt rise in all three line ratios off the nucleus along the minor axis is evident in Figures 6*a*–6*c*. In particular, [O I]/Hα reaches values of 20%–30%, and both [N II]/Hα and [S II]/Hα exceed unity at some locations. The difference in behavior between the minor- and major-axis line ratios is most evident in [N II] (Figs. 6*a* and 6*d*) since the [N II]/Hα ratio remains low and remarkably constant out to a

TABLE 1

OPTICAL SPECTRA

Position (1)	[O III] λ5007/Hβ (2)	[O I] λ6300/Hα (3)	[N II] λ6584/Hα (4)	[S II]/Hα (5)	Hα/Hβ (6)
Nuclear	≤ −0.18	−1.48	−0.31	−0.52	≤ +1.17
Off-nuclear minor-axis	≤ +0.07	−1.00	−0.11	−0.30	≤ +1.03
Off-nuclear major-axis	≤ −0.27	−1.53	−0.43	−0.53	≤ +0.98

NOTES.—Col. (1) The location of the one-dimensional spectra extracted from the low-resolution long-slit data. The nuclear spectrum is taken from the central ∼12″ of the P.A. = 40° spectrum. The off-nuclear minor-axis spectrum is taken from the regions ∼6″–28″ northeast and ∼15″–25″ southwest of the nucleus along the P.A. = 40° spectrum. The off-nuclear major-axis spectrum is taken from the regions ∼11″–24″ southeast and ∼22″–29″ northwest of the nucleus along the P.A. = 133° spectrum. Cols. (2)–(6) The log of the observed emission-line flux ratio. The values in cols. (2) and (6) are upper limits due to the effect of an underlying Hβ stellar absorption line. The value in col. (5) refers to the sum of the [S II] λλ6717 + 6731 emission lines relative to Hα.

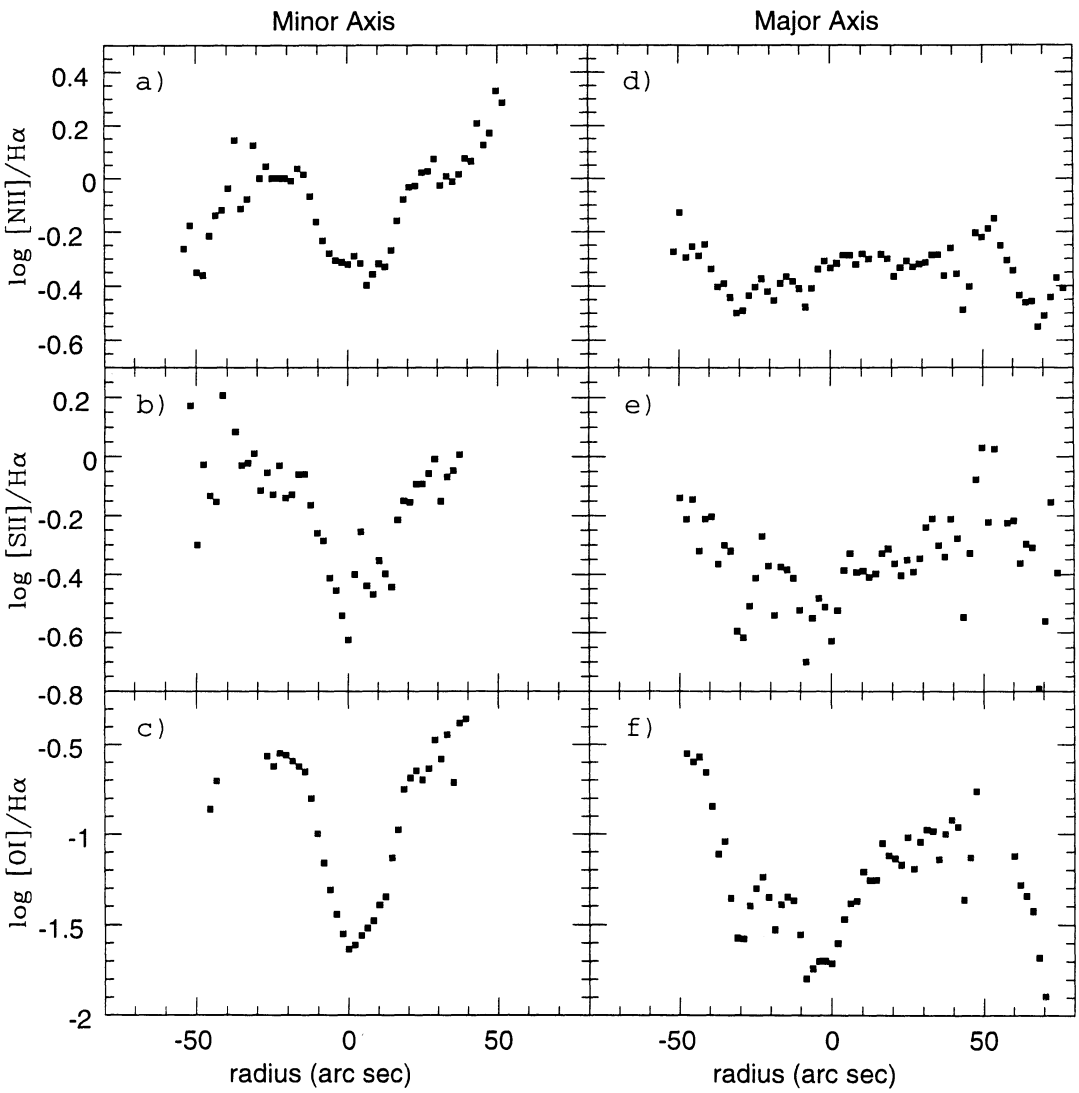

FIG. 6.—Optical [N II]/Hα, [S II]/Hα, and [O I]/Hα emission-line flux ratios as a function of radius measured from the high-resolution long-slit data. Panels (*a*)–(*c*) are along the galaxy minor axis, where negative radii are positions northeast of the nucleus and positive radii are positions southwest of the nucleus. The strong H II–region emission ∼30″ northeast of the nucleus has been excluded from these plots to highlight the gas associated with the outflowing wind. Panels (*d*)–(*f*) are along the galaxy major axis, where negative radii are positions southeast of the nucleus and positive radii are positions northwest of the nucleus. The ionized gas along the minor axis exhibits a steep rise in all three emission-line flux ratios 10″–15″ off the nucleus, indicating the importance of shock heating away from the nuclear starburst. The difference in behavior between the minor- and major-axis line ratios is most evident in [N II] ([*a*] and [*d*]) since the [N II]/Hα ratio remains low and remarkably constant out to a radius of nearly 50″ (3.6 kpc).

radius of nearly 50″ (3.6 kpc). While some locations along the major axis do have stronger line flux ratios than at the nucleus itself (see Figs. 6*e* and 6*f*), most have ratios that are a factor of 2–3 smaller than those seen along the minor axis at the same radius.

In Figure 7 we show a nuclear and an off-nuclear minor-axis spectrum of NGC 2146, both covering the 6300–6800 Å region. The nuclear spectrum in Figure 7*a* is from the central 2″ of the high-resolution long-slit data. The off-nuclear minor-axis spectrum in Figure 7*b* is the sum of the regions 15″–26″ northeast and 17″–28″ southwest of the nucleus. These two spectra illustrate the very different emission-line signatures of the nuclear and off-nuclear gas in NGC 2146.

The high-resolution spectra also allow us to measure the radial variation in the electron density, using the [S II] λ6717/λ6731 doublet ratio (e.g., Osterbrock 1989). The density drops from a central value of $\sim$200 cm^{-3} to the low-density limit (less than 100 cm^{-3}) at radii greater than $\sim$10″ ($\sim$700 pc). The implied central gas pressure (for log T = 4.0) is approximately 6×10^{-10} dyn cm^{-2}. The values for the central density and pressure and the radial decline in density and pressure are typical of starburst galaxies which are known to be driving outflowing winds (cf. Heckman, Armus, & Miley 1990; Lehnert & Heckman 1994). The models of ram-pressure–driven winds presented in Heckman et al. (1990) predict, when applied to NGC 2146, a total thrust in the wind at a radius of 10″ of $\sim 10^{34}$ dyn.

Perhaps the most interesting insight provided by the new spectral data concerns the kinematics and dynamics of the gas in the region of X-ray emission. Along the minor axis we see a velocity shear of $\sim$130 km s^{-1}. This gradient can be seen in Figure 8 (Plate 20), where we display the full two-dimensional minor-axis spectrum, highlighting the Hα + [N II] emission-line complex. The gas is predominantly blueshifted to the northeast and redshifted to the southwest. This is as expected for an outflow, since from the morphology of the galaxy's dust lane we know that the northeast is the near side of the disk. Along the major axis we obtain a rotation curve in satisfactory agreement with those published by Hutchings et al. (1990) and Prada et al. (1994). Although difficult to see in Figure 8, the

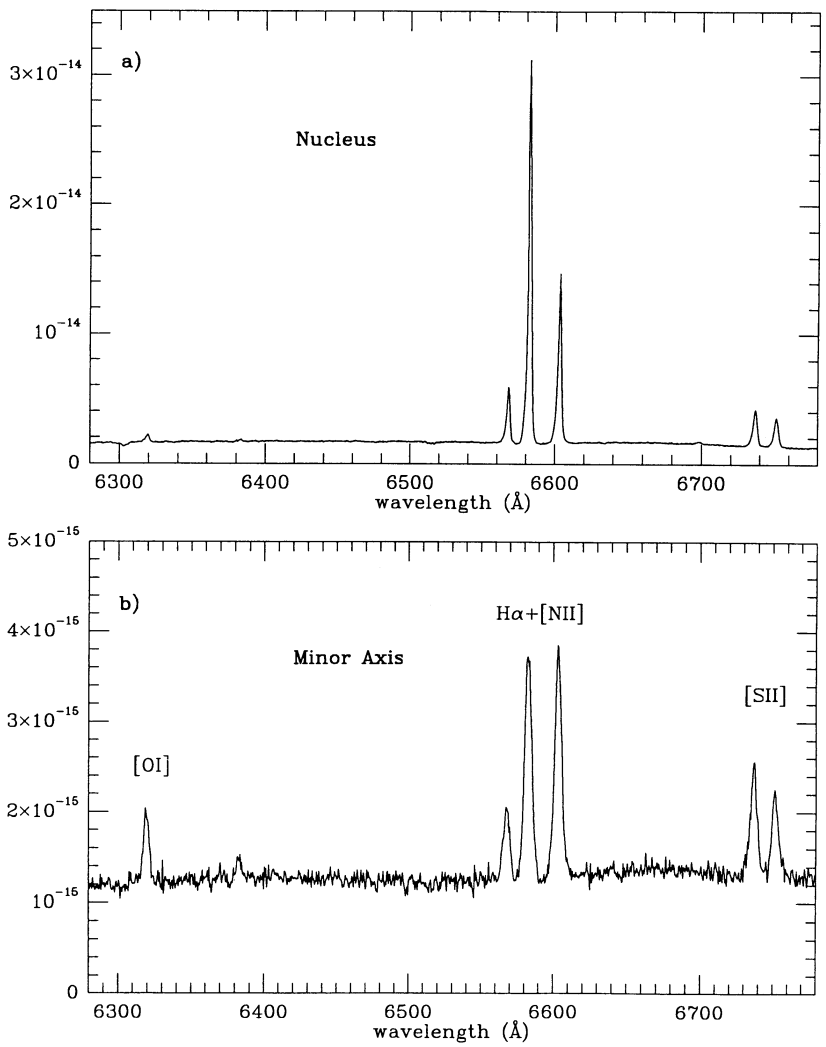

FIG. 7.—One-dimensional (*a*) nuclear and (*b*) off-nuclear minor-axis spectra of NGC 2146 covering the 6300–6800 Å region. The ordinate is plotted in units of ergs cm^{-2} s^{-1} Å^{-1}. The nuclear spectrum in (*a*) has been extracted from the central 2″ of the high-resolution long-slit data. The minor-axis spectrum in (*b*) is the sum of the regions 15″–26″ northeast and 17″–28″ southwest of the nucleus. These data illustrate the varying emission-line flux ratios and line widths (see Fig. 9) traced in Figs. 6*a*, 6*b*, and 6*c*, showing the very different spectra present in the nuclear starburst as compared to the outflowing minor-axis superwind.

1995ApJ...445..666A

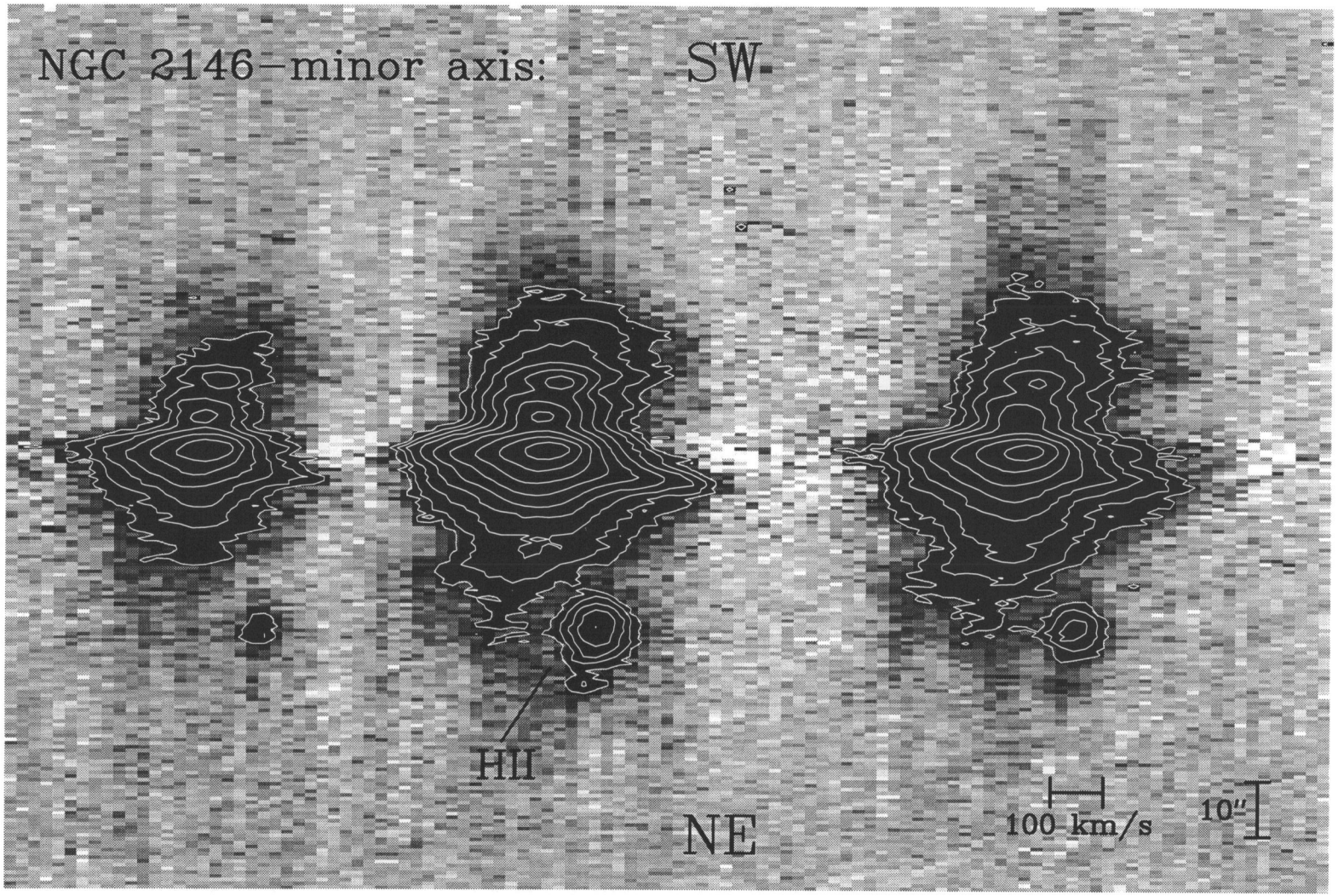

FIG. 8.—Gray-scale representation of the Hα + [N II] complex in the high-resolution, two-dimensional, minor-axis long-slit data. The continuum emission has been subtracted to produce a "pure" emission-line spectrum. Northeast is toward the bottom of the image, while southwest is toward the top. Wavelength increases toward the right. Two bars indicating both a spatial scale of 10″ and a kinematic scale of 100 km s^{-1} are in the lower right of the figure. Note the strong blue gradients in the emission lines from southwest to northeast. The bright knot ~30″ northeast of the nucleus is an H II–region hotspot in the string of H II regions visible in Fig. 3. This knot is labeled as "HII" here.

ARMUS et al. (see 445, 674)

[N II] and Hα lines appear to be split over the regions 25″–45″ northeast and 20″–45″ southwest of the nucleus. These correspond to projected physical scales of ∼1.5–3.1 kpc. The line splittings are ∼150–200 km s^{-1}.

In Figure 9 we show the variation in the width of the [N II] λ6584 emission line as a function of position along both the major and minor axes. The line width increases dramatically along the minor axis—from only ∼100 km s^{-1} on the nucleus to typically 200–300 km s^{-1} at radii ≥15″ (∼1 kpc). In contrast, the lines remain relatively narrow (100 ± 50 km s^{-1}) along the major axis. This behavior is very similar to that exhibited by the emission-line flux ratios in Figure 6. This implies that there is a good correlation between the emission-line widths and flux ratios. This can be seen explicitly in Figure 10 and suggests that there is a coupling between the physical and dynamical state of the ionized gas (cf. Lehnert & Heckman 1995, who find this a general property of infrared-loud starburst galaxies). Such a coupling is consistent with a picture in which the gas in the starburst and along the galactic major axis is relatively quiescent material being photoionized by hot stars, while the gas along the minor axis is being accelerated and shock-heated by an outflowing wind.

Additional evidence for an outflow is provided by the profiles of the emission lines and the Na I D absorption-line doublet in the central region of the galaxy. AHM89 have shown that the Na I D line is almost always interstellar rather than stellar in origin in infrared-bright, starburst galaxies like NGC 2146. The nuclear Hα and [N II] emission-line profiles are shown in Figure 11. They are blue-asymmetric in form, extending to velocities of −300 to −400 km s^{-1} with respect to the line core. In the case of the absorption-line profile, the interpretation in terms of an outflow is unambiguous (cf. Phillips 1993). In the case of the emission lines, a blue-asymmetric profile will be produced by an outflow if the backside (redshifted gas) is hidden from view by dust.

4. DISCUSSION

4.1. *Physical Parameters*

As discussed in § 3.2 above, our *ROSAT* PSPC spectrum can be well fitted by a two-component model. PSPC images constructed from the energy channels in which each of the two spectral components should dominate also have significantly different morphologies (see Fig. 5). The "hard" component (which can be fit as thermal emission with $kT \gg 1$ keV) dominates the PSPC counts in the energy ranges both above 1 keV and below 600 eV, and the "soft" component which is almost certainly thermal emission with $kT = 300$–600 eV [$T \sim (3.5–7) \times 10^6$ K] dominates the PSPC counts in the 600 eV to 1 keV energy range where the spectral feature we identify as the Fe L emission complex (including the resonance lines of the hydrogenic and He-like ions of O and Ne) is very strong.

The luminosity of the soft component (∼10^{40} ergs s^{-1} in the 0.1–2.4 keV band for $N_H = 0$), implies that the volume integral of the density squared for the gas producing this luminosity is $\sim 4 \times 10^{62}$ cm^{-3}. Half of this integral is represented by gas interior to a radius of ∼0.5, or ∼2.2 kpc (the "inner region"), and the rest is represented by the gas located between radii of ∼0.5 and 2.5, or ∼2.2–10.7 kpc (the "outer region"). We adopt a volume filling factor for the X-ray–emitting gas of f (e.g., $f \leq 1$) and now proceed to compute several of the most important physical parameters for the *soft* component.

1. We find that the mean gas density is $1.3 \times 10^{-2} f^{-1/2}$ cm^{-3} in the inner region and $1.1 \times 10^{-3} f^{-1/2}$ cm^{-3} in the outer.

2. For $T = 5 \times 10^6$ K, the corresponding pressures are $P(\text{soft}) \sim 2nkT = 1.8 \times 10^{-11} f^{-1/2}$ dyn cm^{-2} in the inner region and $P \sim 1.5 \times 10^{-12} f^{-1/2}$ dyn cm^{-2} in the outer. Our optical spectra imply that the mean pressure in the emission-line gas inside $r = 2.2$ kpc is $\leq 4 \times 10^{-10}$ dyn cm^{-2}. This is consistent with our estimated pressure for the X-ray–emitting gas unless its volume filling factor is very small (i.e., f must be greater than 2×10^{-3} for consistency).

3. The mass of the gas is $1.3 \times 10^7 f^{1/2}\ M_\odot$ in the inner region and $1.5 \times 10^8 f^{1/2}\ M_\odot$ in the outer region.

4. The thermal energy contents are $3.2 \times 10^{55} f^{1/2}$ ergs and $3.8 \times 10^{56} f^{1/2}$ ergs in the inner and outer bins, respectively.

5. The radiative cooling times for the gas are given by $t(\text{cool}) = 3kT/\Lambda n$, where $\Lambda = 3.5 \times 10^{-23}$ ergs cm^3 s^{-1} for gas with solar abundances and $T \sim 5 \times 10^6$ K (R. Sutherland 1994, private communication). This yields values for t(cool) of $1.5 \times 10^8 f^{1/2}$ yr in the inner region and $1.7 \times 10^9 f^{1/2}$ yr in the outer region.

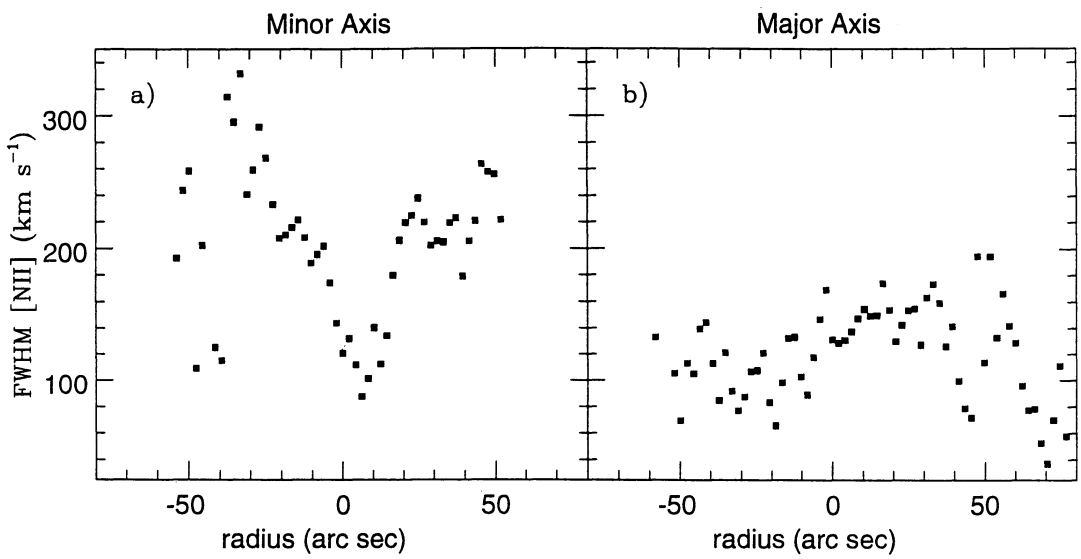

FIG. 9.—Variation of the FWHM of the [N II] λ6584 emission line with radius along both the minor and major axes of the high-resolution long-slit data. There is a dramatic increase in the line width of the nucleus along the minor axis, from about 100 to 300 km s^{-1}, which is not evident along the major axis.

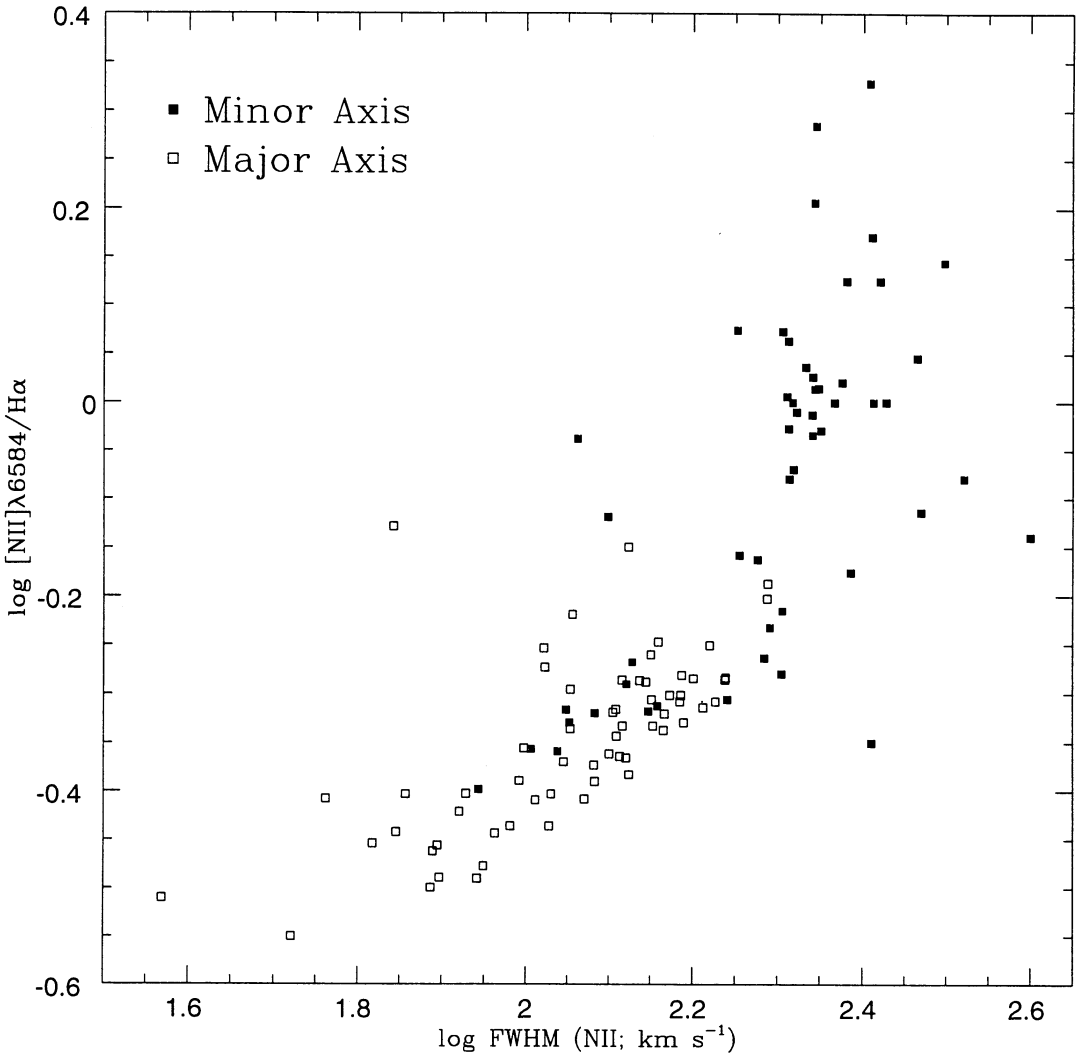

FIG. 10.—Relationship between the [N II] λ6584/Hα emission-line flux ratio and the FWHM of the [N II] line along the major (*open squares*) and minor (*filled squares*) axes. Along the minor axis, the gas with the largest [N II]/Hα line flux ratios (shock-heated) also exhibits the widest lines (~250–300 km s^{-1}); hence, the physical and dynamical state of the gas involved in the outflow is coupled. Plots of the [S II] and [O I] lines are qualitatively similar.

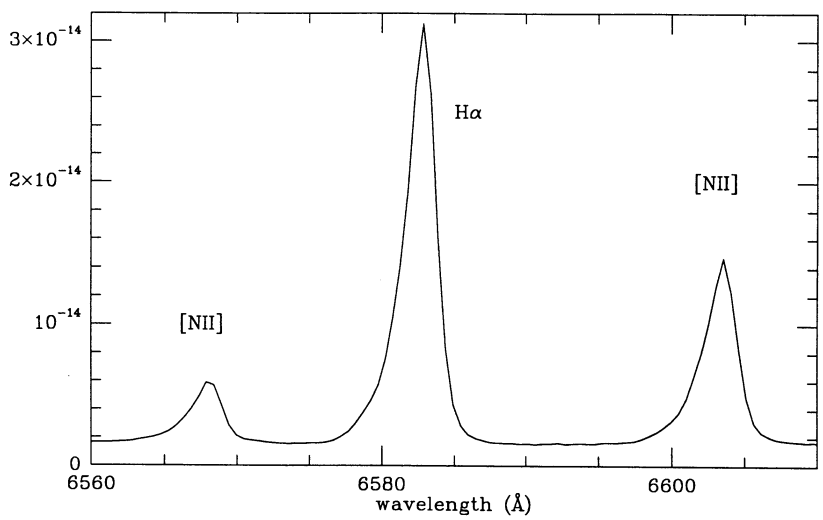

FIG. 11.—Enlargement around the Hα + [N II] complex of the nuclear (central 2″) spectrum from the high-resolution data. The ordinate is plotted in units of ergs cm^{-2} s^{-1} Å^{-1}. The emission lines in the nucleus exhibit asymmetric wings that extend ~300–400 km s^{-1} blueward of the systemic velocity.

The spectral properties (and hence the nature) of the hard component are not well constrained by our data, owing to the soft energy range covered by the *ROSAT* PSPC. Following the BBXRT and *ASCA* results on the starburst galaxies M82 and NGC 253 (Petre 1993), if we assume that the hard component is thermal emission from hot gas, we can make similar calculations for its physical parameters. Note however that we later show (see § 4.2) that the model underestimates the luminosity of the hard spectral component if it is hot gas associated with the outflowing superwind. The temperature for this component is $kT > 2.2$ keV ($T > 2.6 \times 10^7$ K). Since the emissivity of thermal gas in the *ROSAT* band is roughly constant in the temperature range $kT \sim 2$–10 keV, the luminosity of the hard thermal component in the 0.1–2.4 keV band ($\sim 2 \times 10^{40}$ ergs s^{-1} for $N_H = 0$) implies that the volume integral of its density squared is 1.7×10^{63} cm^{-3}, roughly independent of temperature. Using this value, and the lower limit to T, we can derive the following values and limits for the physical properties of a *hard* thermal component:

1. The implied gas densities are $2.7 \times 10^{-2} f^{-1/2}$ cm^{-3} in the inner region and $2.3 \times 10^{-3} f^{-1/2}$ cm^{-3} in the outer region.
2. For $T > 2.6 \times 10^7$ K, the corresponding pressures are greater than $1.7 \times 10^{-10} f^{-1/2}$ dyn cm^{-2} and greater than $1.4 \times 10^{-11} f^{-1/2}$ dyn cm^{-2}. The pressure in the inner region is consistent with our optically determined pressure if the filling factor of the hot gas producing the hard component is greater than 20%.
3. The implied gas masses are $2.7 \times 10^7 f^{1/2}$ $M_\odot$ and $3.1 \times 10^8 f^{1/2}$ $M_\odot$ in the inner and outer regions, respectively.
4. For $T > 2.6 \times 10^7$ K, the corresponding thermal energy contents are greater than $3.4 \times 10^{56} f^{1/2}$ ergs in the inner region and greater than $4 \times 10^{57} f^{1/2}$ ergs in the outer region.
5. The implied radiative cooling times (for $\Lambda = 1.8 \times 10^{-23}$ ergs cm^3 s^{-1} at $T = 2.6 \times 10^7$ K) are greater than $7 \times 10^8 f^{1/2}$ yr and greater than $8 \times 10^9 f^{1/2}$ yr for the inner and outer regions, respectively. These are lower limits since the cooling time increases at higher temperatures.

4.2. *Predictions of a Starburst-driven Wind*

A review of the X-ray properties expected for starburst-driven galactic winds is given in HLA93. The hot gas created by the ensemble of supernovae and stellar winds in the starburst drives an expanding bubble-like structure out of the disk and up into the galactic halo. There are then two fluids to be considered as potential sources of thermal X-rays: the tenuous wind fluid itself which fills the bubble, and the ambient halo gas with which the wind-driven bubble interacts.

The temperature of shock-heated gas is related to the shock velocity by the relation $kT = (3/16)\mu m_H v(\text{shock})^2$, where μm_H is the mean mass per particle just downstream of the shock. Since the shocked fluid is predicted to be fully ionized and to have an outflow speed velocity of up to 3000 km s^{-1} (cf. Chevalier & Clegg 1985; HLA93), the temperature for internal shocks in the wind will be up to $\sim 10^8$ K. As the wind hits the relatively dense ambient gas, it will drive a slower shock into this gas. For $T \sim 5 \times 10^6$ K, as observed for the soft component in NGC 2146, the implied shock speeds are ~ 600 km s^{-1}.

4.2.1. *Outflow Pressures*

The mean values for the pressures predicted for a superwind arising from a starburst depend first upon the kinetic energy input rate from the starburst, which is estimated to be $dE/dt \sim 3 \times 10^{42}$ ergs s^{-1} for NGC 2146 based on the relations given in Leitherer & Heckman (1995). If we are dealing with a freely expanding wind, the relevant quantity is the wind's ram pressure:

$$P = 5.6 \times 10^{-10} (dE/dt_{43}) r^{-2} \text{ dyn cm}^{-2}, \quad (1)$$

where dE/dt_{43} is the energy injection rate in units of 10^{43} ergs s^{-1}, r is the radius in kiloparsecs, and we have assumed a wind velocity of ~ 3000 km s^{-1}. The predicted ram pressures are then $\sim 2 \times 10^{-10}$ dyn cm^{-2} in the inner region and $\sim 5 \times 10^{-12}$ dyn cm^{-2} in the outer region. We have made these rough estimates at radii corresponding to the midpoints of the inner and outer regions.

In the case that the wind is not free and is inflating an adiabatic windblown bubble, the characteristic pressure is $\sim 10/33$ times the total kinetic energy injected by the wind divided by the bubble volume (cf. Koo & McKee 1992 for a more detailed treatment). The equations of motion for a windblown adiabatic bubble (see below) expanding into a uniform galactic halo with density n_{-3} (in units of 10^{-3} cm^{-3}) for a time t_7 (in units of 10^7 yr) then imply

$$P = 8 \times 10^{-12} (dE/dt_{43})^{2/5} n_{-3}^{3/5} t_7^{-4/5} \text{ dyn cm}^{-2}. \quad (2)$$

The X-ray pressures estimated in § 4.1 above are therefore consistent with those expected for a wind if the filling factor is of order 1%–10% for the soft source. If the hard source is thermal emission from hot gas associated with the wind, it would have to have a filling factor near unity for its pressure to come close to the predictions.

4.2.2. *Outflow Timescales*

For the predicted kinetic energy flux in the wind of $\sim 3 \times 10^{42}$ ergs s^{-1}, the thermal energy content of the gas could be supplied by the wind over a timescale $t(\text{heat}) \sim 4 \times 10^6 f^{1/2}$ yr for the soft component and $\geq 4.7 \times 10^7 f^{1/2}$ yr for the hard component (for $T > 2.6 \times 10^7$ K). These timescales can be compared to the age of the outflow. The expanding bubble model predicts that the shock speed we derived for the soft component (~ 600 km s^{-1}) corresponds roughly to the expansion speed of the bubble's outer shell. Thus, the dynamical age is $t(\text{dyn}) \sim 10.7$ kpc/600 km s^{-1} $\sim 2 \times 10^7$ yr. This value is quite similar to the typical ages deduced from detailed modeling of the stellar content of starbursts similar to NGC 2146 (e.g., Bernlohr 1993a, b; Rieke et al. 1993). We thus conclude that a starburst-driven wind operating over a timescale of a few $\times 10^7$ yr could easily heat the gas associated with the soft component, but could only heat the gas associated with the hard component if this gas has a temperature close to the minimum allowed (2.6×10^7 K).

4.2.3. *Predicted Temperatures and Luminosities*

The bolometric radiant luminosities of the hard and soft components ($\sim 2 \times 10^{40}$ ergs s^{-1} for $kT = 10$ keV for the hard component, and $\sim 10^{40}$ ergs s^{-1} for the soft component, for the models described in § 3.2) are much less than the kinetic energy flux predicted for the wind (by about two orders of magnitude). Thus, the wind does not appear to be suffering significant radiative cooling by X-rays, even if the hard X-ray source is powered by the wind. We conclude that radiative losses can probably be ignored in considering the dynamical and thermal state of the X-ray–emitting gas.

Since the X-ray–emitting region is therefore probably adiabatic, we can make estimates of the predicted X-ray emission for an expanding windblow bubble (from both the hot wind material inside the bubble and from the shocked ambient gas

in the outer shell of the bubble). We will assume that the wind is expanding into a galactic halo of uniform density.

The classic paper of Castor, McCray, & Weaver (1975) derived simple expressions for the dynamical evolution of an adiabatic bubble inflated into a medium of constant density by a constant rate of kinetic energy injection. In this model, the windblown bubble consists of five concentric zones: (1) the innermost region within which the mass and kinetic energy are injected (the starburst in this case), (2) a region of a supersonic wind, (3) a region of hot gas which represents outflowing wind material from zone 2 that has passed through the shock that separate zones 2 and 3, (4) a shell of swept-up ambient gas that has been shock-heated and accelerated as zone 3 expands outward, and (5) the umperturbed ambient medium (here the galactic halo). Two potential sources of spatially resolved X-ray emission are then the hot, shocked wind material in zone 3 and the shocked halo gas in zone 4. Let us consider the predicted X-ray properties of these two regions in turn.

We can roughly estimate the properties of the X-ray emission from the hot gas inside the superwind-blown bubble (zone 3) in the following manner. First, we use Castor et al.'s expression for the bubble's radius (see eq. [7] below) to derive the bubble volume. We then assume that the bubble's interior is filled uniformly and solely by the hot gas injected directly by the supernovae and stellar winds in the starburst. This means that we are ignoring the (possibility significant) contribution of evaporated material inside the bubble. In this sense our estimate is a lower bound on the X-ray luminosity from the bubble interior. We expect the starburst wind speed (in zone 2) to substantially exceed the expansion velocity of the outer shell of the windblown bubble (zone 4): these velocities are expected to be several thousand and several hundred km s^{-1}, respectively (HLA93). In this case, the shocked-wind region (zone 3) will occupy most of the interior of the bubble (the free-wind region of zone 2 will occupy very little relative volume—cf. Koo & McKee 1992).

The temperature of the gas in zone 3 will be given by

$$T = (10/33)k^{-1}\mu m_{\rm H}(dE/dt)(dM/dt)^{-1} , \quad (3)$$

where dM/dt is the mass outflow rate in the wind. This implies that $kT \sim 7$ keV for the predicted v(wind) of 3000 km s^{-1} appropriate for a starburst-driven outflow (cf. Chevalier & Clegg 1985; Suchkov et al. 1994; Leitherer & Heckman 1995). Taking the emissivity in the *ROSAT* PSPC band to be $\sim 9 \times 10^{-24}$ ergs cm^3 s^{-1} for $kT = 7$ keV the implied X-ray luminosity of zone 3 of the bubble is just

$$L = 1.65 \times 10^{38}(dE/dt_{43})^{7/5}n_{-3}^{3/5}t_7^{1/5} \text{ ergs s}^{-1} . \quad (4)$$

The X-ray temperature and luminosity of the shell (zone 4 = shocked halo gas) can be estimated assuming that the temperature is $kT = (3/16)\mu m_{\rm H} v(\text{shell})^2$ (see above) and that its density is 4 times the density of the halo (strong adiabatic shock). The equations of motion for the windblown shell (cf. Castor et al. 1975; HLA) then give v(shell), which in turn implies

$$T(\text{shell}) = 6 \times 10^6(dE/dt_{43})^{2/5}n_{-3}^{-2/5}t_7^{-4/5} \text{ K} , \quad (5)$$

Provided that the shell is adiabatic (has $L \ll dE/dt$), and has a temperature in the range log $T = 5.9$–7.3 (where the emissivity in the *ROSAT* band is approximately independent of temperature), its X-ray luminosity in the *ROSAT* PSPC band can be approximated (to within a factor of 2) by

$$L(\text{shell}) = 1.5 \times 10^{40}(dE/dt_{43})^{3/5}n_{-3}^{7/5}t_7^{9/5} \text{ ergs s}^{-1} . \quad (6)$$

Finally, the radius of the shocked bubble is predicted to be

$$r(\text{shell}) = 10(dE/dt_{43})^{1/5}n_{-3}^{-1/5}t_7^{3/5} \text{ kpc} . \quad (7)$$

We conclude that equations (5), (6), and (7) describing the shocked halo gas provide a reasonably good match to the temperature, luminosity, and size of the observed "soft" component of X-ray emission in NGC 2146. The temperature predicted for the hot bubble interior is consistent with our measured lower limit to the temperature of the "hard" component. However, equation (4) shows that the same halo parameters would lead to an X-ray luminosity from the bubble interior that is less than 1% of the observed value for the "hard" component.

4.3. *Nature of the Hard Source*

While the properties of the soft component in our PSPC data can be plausibly understood as thermal emission from tenuous gas in the halo of NGC 2146 that has been shock-heated by an outflowing wind, the nature of the hard component is not at all clear. We can briefly summarize some possibilities and the problems associated with each:

1. *Thermal emission from a galactic wind.*—As discussed in more detail in § 4.2, the X-ray luminosity of the hard component is more than two orders of magnitude larger than predicted for the wind for plausible galaxy halo densities (densities that match well the properties of the soft component).

2. *Emission from a population of massive X-ray binaries or young supernova remnants in the starburst.*—Both the size of the emission region and its morphology disagree strongly with the size and morphology of the starburst (see Fig. 3). In fact, we find that only a modest fraction ($\sim$10%–15%) of the emission from the hard component arises from inside the central starburst.

3. *Emission from normal sources not associated with the starburst.*—Even normal (nonstarburst) spiral galaxies are moderately strong hard X-ray sources with typical $L(X) \sim 10^{39}$–10^{40} ergs s^{-1} and kT approximately several keV (cf. Kim, Fabbiano, & Trinchieri 1992; Fabbiano & Trinchieri 1985). The relation between optical and X-ray luminosity for normal spiral galaxies found by Fabbiano & Trinchieri implies that an average spiral with the same absolute blue magnitude as NGC 2146 should have a 0.5–3 keV X-ray luminosity of $\sim 7 \times 10^{39}$ ergs s^{-1}, which is a factor of $\sim$4 below our measured luminosity of NGC 2146 in the 0.2–2.4 keV band. This would make NGC 2146 one of the two most "X-ray–loud" galaxies in their sample of 48 "normal" spirals (which in fact includes starbursts like NGC 253 and NGC 520).

4. *Inverse Compton emission from the galactic wind.*—It has been suggested that the X-ray halo around M82 may be due (at least in part) to inverse Compton scattering of infrared photons from the starburst off the same outflowing relativistic electrons in the halo that produce the radio synchrotron halo (e.g. Schaaf et al. 1989). Arguments against this model in the case of M82 have been given by Seaquist & Odegard (1991), who find that an inverse Compton origin for the X-rays requires the relativistic electron density to be nearly two orders of magnitude above the equipartition value. Moreover, the hard spectral component in the BBXRT data on M82 and NGC 253 cannot be fit by a power-law (inverse Compton) model (Petre 1993). We cannot make this claim for NGC 2146 however.

5. *An optically obscured active galactic nucleus.*—This is ruled out by large size of the X-ray source.

It seems clear that the physical origin of the hard component cannot be elucidated without much better data concerning its spectral and morphological properties. *ASCA* should be able to provide such data (and if not for NGC 2146, then at least for similar systems like M82 and NGC 253).

5. SUMMARY

We have imaged the edge-on starburst galaxy NGC 2146 with the PSPC and the HRI on board *ROSAT* and have compared these data to optical images and long-slit spectra. We can summarize the results below:

1. NGC 2146 possesses a very large X-ray nebula, which is resolved by the PSPC and preferentially oriented along the galaxy minor axis, with a half-light radius of 1′ (4 kpc) and a maximum diameter of ∼4′, or 17 kpc. The total unabsorbed flux is 1.1×10^{-12} ergs cm^{-2} s^{-1} over 0.2–2.4 keV implying a luminosity of $\sim 3 \times 10^{40}$ ergs s^{-1}. Both the absolute size of the X-ray source and its size relative to the central starburst are similar to the corresponding properties of the X-ray emission associated with the outflows in M82 (Fabbiano 1988; Watson, Stanger, & Griffiths 1984), NGC 253 (Fabbiano 1988; Pietsch 1993), and NGC 3628 (Fabbiano et al. 1990; Dahlem et al. 1995).

2. The inner X-ray nebula is itself resolved by the HRI into at least four bright knots together with strong diffuse emission responsible for at least 50% of the flux within a radius of 0.5 (∼2 kpc). The brightest knot has a luminosity of (2–3) $\times 10^{39}$ ergs s^{-1}. The X-ray nebula mapped by the HRI has a spatial extent much larger than the starburst ridge seen at centimeter wavelengths by Kronberg & Biermann (1981) and is oriented in an "X-like" pattern along the galaxy minor axis.

3. The minor-axis X-ray emission is associated with a region of Hα and dust filaments seen in optical images. Optical spectra show that the emission-line gas here is characterized by relatively broad lines (∼250 km s^{-1} FWHM) and by "shocklike" emission-line flux ratios. Together with the blue-asymmetric nuclear emission-line and NaD interstellar absorption-line profiles, these optical data strongly suggest the presence of a starburst-driven superwind.

4. The X-ray spectrum extracted from the central 5′ contains a strong Fe L emission-line complex at 0.6–1.0 keV and a hard excess above 1.0 keV. The spectrum is best described with a two-component model, containing a soft ($kT \sim 400$–500 eV) Raymond-Smith thermal plasma together with either a $\Gamma = 1.7$ power-law or a $kT > 2.2$ keV bremsstrahlung component. The soft thermal component provides ∼30% of the total luminosity over 0.2–2.4 keV, or $\sim 10^{40}$ ergs s^{-1}. The pressure derived from the soft component of the X-ray spectrum is consistent with that predicted from a starburst-driven superwind if the filling factor of this gas is ∼1%–10%. Predictions of the luminosity, temperature, and size of an adiabatic starburst-generated windblown bubble are consistent with those measured for the soft thermal X-ray emission in NGC 2146. If the hard X-ray component is thermal gas associated with the galactic outflow, however, the filling factor must be close to unity. This emission has a luminosity much larger than that predicted by the superwind model if it represents thermal emission from gas heated by an internal shock in the expanding bubble. Possibilities for this hard component are a collection of sources (binaries, supernova remnants, etc.) associated with the starburst or the old preexisting stellar population, inverse Compton emission associated with infrared photons scattered off relativistic electrons convected into the halo by the outflowing wind, or an optically obscured active galactic nucleus. While the first three possibilities are all plausible in light of the nature of NGC 2146, the latter seems unlikely given the size of the X-ray nebula and the starburst nuclear spectrum. The origin of the hard X-ray spectral component will become clearer with high-quality X-ray data which will become available from such space missions as *ASCA*.

We would like to thank Joel Bregman, Julian Krolik, Richard Mushotzky, Rob Petre, Jane Turner, and Meg Urry for helpful comments and suggestions. Diane Gilmore and James Larkin provided a great deal of help with the data reduction and the production of the figures, and both are greatly appreciated. The research described here was supported through NASA grant NAG 5-1861. M. D. L. would like to thank KPNO for the generous allocation of observing time, and its staff, especially Kurt Loken and Kevin Schramm, for expert assistance at the telescope. The work of M. D. L. at IGPP/LLNL was performed under the auspices of the US Department of Energy under contract W-7405-ENG-48. This research has made use of the NASA/IPAC Extragalactic Database which is operated by the Jet Propulsion Laboratory, Caltech, under contract with NASA.

REFERENCES

Armus, L., Heckman, T. M., & Miley, G. K. 1989, ApJ, 347, 727 (AHM89)
———. 1990, ApJ, 364, 471
Benvenuti, P., Capaccioli, M., & D'Odorico, S. 1975, A&A, 41, 91
Bernlohr, K. 1993a, A&A, 268, 25
———. 1993b, A&A, 270, 20
Bevington, P. R. 1969, Data Reduction and Error Analysis for the Physical Sciences (New York: McGraw-Hill)
Burstein, D., & Heiles, C. 1982, AJ, 87, 1165
Castor, J., McCray, R., & Weaver, R. 1975, ApJ, 200, L107
Chevalier, R. A., & Clegg, A. W. 1985, Nature, 317, 44
Dahlem, M., Heckman, T. M., Fabbiano, G., & Gilmore, D. 1995, in preparation
Fabbiano, G. 1988, ApJ, 330, 672
Fabbiano, G., Heckman, T. M., & Keel, W. C. 1990, ApJ, 355, 442
Fabbiano, G., & Trinchieri, G. 1984, ApJ, 286, 491
Hasinger, G., Turner, T. J., George, I. M., & Boese, G. 1992, Legacy, 2, 77
Heckman, T. M., Armus, L., & Miley, G. K. 1990, ApJS, 74, 833
Heckman, T. M., Lehnert, M. D., & Armus, L. 1993, in The Evolution of Galaxies and Their Environments, ed. S. M. Shull & H. Thronson (Dordrecht: Kluwer), 455 (HLA93)
Hutchings, J. B., Neff, S. G., Stanford, S. A., Lo, E., & Unger, S. W. 1990, AJ, 100, 60
Kim, D.-W., Fabbiano, G., & Trinchieri, G. 1992, ApJ, 393, 134
Koo, B.-C., & McKee, C. 1992, ApJ, 388, 103
Kronberg, P. P., & Biermann, P. 1981, ApJ, 243, 89
Lehnert, M. D., & Heckman, T. M. 1995, ApJS, 97, 89
Lehnert, M. D., et al. 1995, in preparation
Leitherer, C., & Heckman, T. M. 1995, ApJS, 96, 9
Osterbrock, D. E. 1989, Astrophysics, of Gaseous Nebulae and Active Galactic Nuclei (Mill Valley: University Science)
Peitsch, W. 1993, in The Physics of Nearby Galaxies: Nurture or Nature? ed. T. X. Thuan, C. Balkowski, & J. T. T. Van (Paris: Editions Frontieres), 67
Petre, R. 1993, in The Nearest Active Galaxies, ed. J. Beckman, L. Colina, & H. Netzer (Madrid: Consejo Superior de Investigaciones Cientificas), 117
Phillips, A. C. 1993, AJ, 105, 486
Prada, F., Beckman, J. E., McKeith, C. D., Castles, J., & Greve, A. 1994, ApJ, 423, L35
Raymond, J. C., & Smith, B. 1977, ApJS, 35, 419
Rieke, G. H., Loken, K., Rieke, M. J., & Tamblyn, P. 1993, ApJ, 412, 99
Schaaf, R., Petisch, P., Biermann, P., Kronberg, P. P., & Schmutzler, T. 1989, ApJ, 336, 732
Schlegel, E. M. 1994, ApJ, 424, L99
Seaquist, E., & Odegrad, N. 1991, ApJ, 369, 320
Shafer, R. A., Haberl, F., & Arnaud, K. A. 1989, in XSPEC: An X-Ray Spectral Fitting Package (ESA TM-09; Paris: ESA)
Suchkov, A., Balsara, D., Heckman, T. M., & Leitherer, C. 1994, ApJ, 430, 511
Veilleux, S., & Osterbrock, D. E. 1987, ApJS, 63, 295
Watson, M., Stanger, V., & Griffiths, R. 1984, ApJ, 286, 144
Young, J. S., Claussen, M. J., Kleinmann, S. G., Rubin, V. C., & Scoville, N. 1988, ApJ, 331, L81